Federal State Autonomous Educational Institution of Higher Education
«Moscow Institute of Physics and Technology» (National Research University)
Landau Phystech School of Physics and Research
Chair for Problems in theoretical physics

Landau Institute for Theoretical Physics (Russian Academy of Sciences)

Major of study: 03.03.01 Applied Mathematics and Physics
Academic specialization: General and Applied Physics

TRANSPORT PROPERTIES OF DISORDERED WEYL SEMIMETALS

(Bachelor's thesis)

Student:
M. E. Ismagambetov

Scientific supervisor:
Dr. P. M. Ostrovsky

Moscow 2022

Annotation

Weyl semimetal is a solid material with isolated touching points between conduction and valence bands in its Brillouin zone—Weyl points. Low energy excitations near these points exhibit a linear dispersion and act as relativistic massless particles. Weyl points are stable topological objects robust with respect to most perturbations. We study effects of weak disorder on the spectral and transport properties of Weyl semimetals in the limit of low energies. We use a model of Gaussian white-noise potential and apply dimensional regularization scheme near three dimensions to treat divergent terms in the perturbation theory. In the framework of self-consistent Born approximation, we find closed expressions for the average density of states and conductivity. Both quantities are analytic functions in the limit of zero energy. We also include interference terms beyond the self-consistent Born approximation up to the third order in the disorder strength. These interference corrections are stronger than the mean-field result and non-analytic as functions of energy. Our main result is the dependence of conductivity on the electron concentration $\sigma = \sigma_0 + An^{1/3} + (B/\sigma_0)n^{2/3} \ln |n|$ with $A \approx -0.142$ and $B \approx 0.018$.

Contents

1 Introduction **4**

2 Statement of the problem **7**

3 Self-consistent Born approximation **10**
3.1 Density of states 11
3.2 Conductivity 11

4 Interference corrections **14**
4.1 Density of states 14
4.2 Conductivity 17
4.2.1 Diagrams with two crossed impurity lines 17
4.2.2 Diagrams with three crossed impurity lines 20

5 Summary and discussion **25**

A Polarization operator **26**

Bibliography **29**

1 Introduction

In 1928, Paul Dirac proposed [1] the first successful description of relativistic electrons using quantum mechanics approach—the celebrated Dirac equation. This equation not only provides the relativistic quantum description of electrons but also predicts the existence of positrons. The Dirac equation is equally suitable for other quantum particles with spin 1/2. One year later, Hermann Weyl pointed out [2] that a simplified version of the Dirac equation for particles with zero mass conserves chirality (projection of spin on the direction of momentum) and hence splits into two independent equations for particles of left and right chirality. For many years, the Weyl equation was a very successful tool for describing neutrinos although since 1998 it is decisively established that neutrinos do have a tiny but nonzero mass [3].

In recent years, the model of massless Weyl fermions has attracted a great attention in condensed matter physics since the discovery of Weyl semimetals. The Weyl semimetal is a solid-state crystal having isolated touching points (Weyl nodes or Weyl points) between conduction and valence bands with low-energy excitations that act as relativistic massless fermions. These fermions are described by the standard Weyl Hamiltonian:

$$H = v\,\boldsymbol{\sigma}\mathbf{p} \tag{1.1}$$

in the vicinity of a Weyl point. Here v is the fixed velocity of massless excitations (in real materials it is a few orders of magnitude lower than the speed of light for the original relativistic Weyl Hamiltonian) and $\boldsymbol{\sigma} = \{\sigma_x, \sigma_y, \sigma_z\}$ is a vector of three standard Pauli matrices.

Each Weyl point has a definite chirality and can be represented as a magnetic monopole, which is a source or sink of Berry flux, see Fig. 1.1. It is known that the net chirality of all touching points in the Brillouin zone must vanish [4] hence there is always an even number of Weyl nodes in the spectrum. As a consequence of the Nielsen-Ninomiya theorem [4], the topological nature of such nodes protects them from opening a gap. Weak perturbations can only shift a Weyl point in momentum or energy while preserving its topological nature. The only possible way to open a spectral gap is by coupling two distant Weyl points. Hence the Weyl semimetal properties are robust with respect to small and smooth perturbations.

Another consequence of the Nielsen-Ninomiya theorem [4] is that no Weyl semimetal is possible in the presence of time reversal ($\mathcal{T}$) and inversion ($\mathcal{P}$) symmetries. Hence there are two kinds of Weyl semimetals with either $\mathcal{T}$ or $\mathcal{P}$ symmetry broken. A Weyl semimetal with broken $\mathcal{T}$ symmetry has at least two Weyl nodes while in the case of broken $\mathcal{P}$ symmetry the minimal number of Weyl nodes is four [7].

An important topological feature of any Weyl semimetal is the existence of low energy surface states that form a Fermi arc [6] connecting projections of Weyl points on the crystal surface (see Fig. 1.1). These states exist on the background of excitationless bulk spectrum since the low energy excitations in the bulk occur only near isolated Weyl points. Fermi arc surface states are very well visible in the momentum-resolved spectroscopic measurements and are used as a hallmark for detecting Weyl semimetals. Recent experiments [8, 9] have

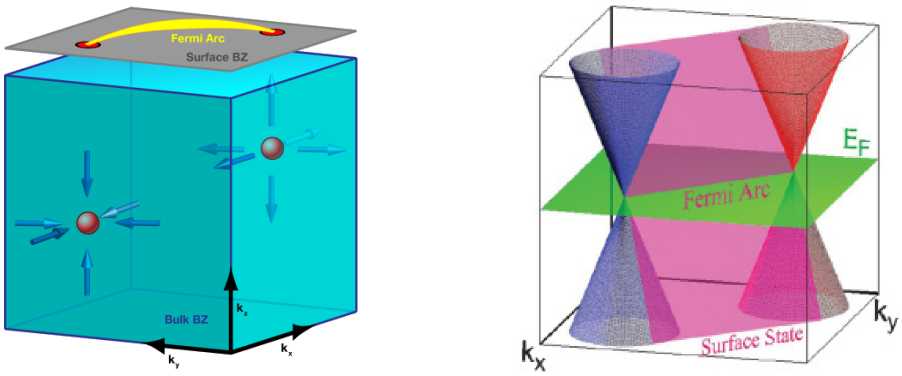

Figure 1.1: (Left) The Brillouin zone of a Weyl semimetal. Weyl nodes are shown as magnetic monopoles for the Berry flux. These points are connected by the Fermi arc on the surface. (Right) Energy-resolved bulk and surface bands in a WSM with zero Fermi energy. Pictures from Refs. [5, 6].

proposed several candidate materials for Weyl semimetals: TaAs, TaP, NbAs, NbP. So far, the best candidate TaAs, studied in Ref. [9], has shown 12 pairs of Weyl nodes.

One of the hottest debated topics in the theory of Weyl semimetals is the proposed quantum phase transition in the low-energy behavior of the density of states. Early numerical simulations of disordered Weyl semimetals [10, 11] have suggested that the density of states at zero energy undergoes a second-order transition from zero to a nonzero value when the strength of potential disorder exceeds a certain threshold. This conclusion is supported by some theoretical analysis. It was shown that a standard perturbation theory in weak disorder [12–15] developed near the dimension $d = 2$ and then continued to $d = 3$ indeed suggests vanishing density of states at zero energy. Alternative consideration in the framework of the nonlinear sigma model [16–18] provided a similar result. At the same time, it is quite clear that even an extremely small probability of a disorder realization that localizes an electron at zero energy is enough to disprove the proposed phase transition [19, 20]. Another nonperturbative approach [21] has suggested that for a broad class of "optimal" fluctuations of disorder potential the density of states is still exactly vanishing. Finally, diagrammatic calculations directly in 3D with Gaussian disorder and different types of momentum cutoff regularization [22, 23] have shown the existence of the phase transition on the level of the mean-field approximation. It can be thus claimed that although a true phase transition in the density of states is hardly possible, there is a very sharp crossover from algebraic to exponentially small density of states as a function of disorder strength [24].

In the present work, we will study disorder effects in a Weyl semimetal in the limit of weak disorder only. Moreover, we will adopt the most standard Gaussian white-noise model of disorder similar to the one considered in Ref. [23]. Technically, this problem is identical to the well-studied Gross-Neveu model [25]. The Gross-Neveu model concerns relativistic particles with point-like instantaneous interaction. In the Euclidean (imaginary time) representation with zero mass and in the limit of zero flavours of the particles, it becomes identical to the Gaussian white-noise disorder model. Taking the limit of zero flavours is needed to eliminate diagrams with fermionic loops, which is equivalent to the replica limit for disordered systems. Critical dimension of the Gross-Neveu model is $d = 2$. Close to this dimension, it is possible to develop a standard perturbative renormalization group approach to take into account logarithmically divergent diagrams. Such calculations were carried out up to the four loop order in Refs. [26, 27]. However, disordered Weyl semimetals correspond to the 3D version of the Gross-Neveu model where strong ultraviolet divergences make the renormalization

group analysis problematic [28].

Massless relativistic excitations appear in a number of other solid-state systems, most notably in graphene [29–33]. Since graphene is essentially a two-dimensional material, disorder effects are well-described by the Gross-Neveu model just in its critical dimension [34–36]. Other common examples of disordered materials with massless spectrum include random bond Ising model [37], critical state at the quantum Hall transition [38], two-dimensional d-wave superconductors [39, 40], and surface states of topological insulators [41].

This work is devoted to 3D Weyl semimetals with weak Gaussian white-noise disorder. As was already pointed out, this model suffers from strong ultraviolet divergences and hence should be properly regularized. We will apply a standard technique of dimensional regularization [42] and allow the dimensionality of the system to deviate from $d = 3$. But contrary to the previous works, we will not perform any expansion near $d = 2$. Instead, we will consider all disorder corrections in a completely arbitrary dimension and do an exact analytic continuation of the results from the region $d < 2$ where ultraviolet divergences are absent to $d = 3$. Since the Gross-Neveu model is not renormalizable in $d = 3$, we will not develop any effective field theory description but instead consider disorder corrections directly to the observable quantities: density of states and conductivity.

Our approach is quite similar to the standard problem of a conventional 3D metal with parabolic spectrum and Gaussian disorder. Detailed analysis of weak disorder effects in this model was performed in Refs. [43, 44]. It was shown that the model exhibits three types of corrections to the conductivity. First, there are corrections of relative strength $\propto (E\tau)^{-1}$, where E is the Fermi energy and τ is the mean free time of the electrons. Second, there are weaker logarithmic corrections $\propto (E\tau)^{-2} \ln(E\tau)$. Such logarithms do not represent truly divergent contributions but require an accurate analysis of the diagrams on a ballistic scale. Finally, there is another logarithmic contribution $\propto (E\tau)^{-2} \log(E/\Delta)$, where Δ is some ultraviolet energy cutoff scale related e.g. to the band width or to the lattice spacing. This type of a logarithmic divergence cannot be resolved in the low energy model with parabolic spectrum and requires an extra parameter Δ. Divergent terms are present both in the conductivity σ and in the total particle density n but cancel out in their ratio, i.e. mobility of the metal $\mu = \sigma/(en)$.

The problem of a disordered Weyl semimetal considered in this work is technically more challenging. We will encounter stronger ultraviolet divergences that can be absorbed into redefinition of model parameters (Fermi energy, disorder strength etc). Such finite renormalizations are automatically taken into account by the dimensional regularization scheme [42]. The remaining logarithmic divergences will be cut at the scale Δ. They do not cancel out in any observable quantity and will constitute an important part of our results.

The structure of the work is the following. In Chapter 2 we formulate the problem and explain some details of the dimensional regularization scheme. Chapter 3 contains the mean-field calculation of the density of states and conductivity based on the self-consistent Born approximation. This approach is similar to Ref. [23]. In Chapter 4 we calculate the diagrams with two and three intersecting impurity lines. We show that these contributions provide nonanalytic corrections to the observable quantities. Main results are summarized and discussed in Chapter 5. Technically intricate details of the calculation of polarization operators in an arbitrary dimension are given in Appendix A.

2 Statement of the problem

We consider a standard model of a single-node Weyl semimetal in the presence of potential disorder described by the following Hamiltonian:

$$H = \boldsymbol{\sigma}\mathbf{p} + V(\mathbf{r}). \tag{2.1}$$

For simplicity, we set the velocity of electrons to unity. In a real Weyl semimetal the number of Weyl nodes is at least two. Our model implies that disorder scattering between these nodes is negligible or, in other words, the disorder potential is smooth on the scale of inverse distance between Weyl nodes in momentum space. Linear momentum dependence of the Hamiltonian is of course also an approximation, that is valid only at low enough energies.

We assume that the random disorder potential obeys the standard Gaussian white-noise statistics

$$\big\langle V(\mathbf{r})\big\rangle = 0, \qquad \big\langle V(\mathbf{r})V(\mathbf{r}')\big\rangle = 2\pi^2\alpha\,\delta(\mathbf{r}-\mathbf{r}'). \tag{2.2}$$

Disorder strength is characterized by a single parameter α, that has a dimension of inverse energy for a 3D problem. The only dimensionless small parameter of our model is

$$\alpha E \ll 1, \tag{2.3}$$

where E is the Fermi energy measured from the Weyl point. All observable quantities are even functions of E so, for definiteness, we assume $E > 0$.

We will calculate average density of states and conductivity of a Weyl semimetal perturbatively in αE using diagrammatic expansion. The unperturbed Green function of the Weyl Hamiltonian is

$$G^{R/A}(E,\mathbf{p}) = \big(E - \boldsymbol{\sigma}\mathbf{p} \pm i0\big)^{-1} = \frac{E + \boldsymbol{\sigma}\mathbf{p}}{(E \pm i0)^2 - p^2}. \tag{2.4}$$

In some parts of the calculation it will be more convenient to use Matsubara representation with imaginary energy $E = i\epsilon$. Retarded/advanced functions are then retrieved by analytic continuation from positive/negative ϵ. For diagrams that involve both types of Green functions we have to keep two different Matsubara energies. Hence it will be convenient to change the sign of the Matsubara energy for advanced Green functions such that analytic continuation is always performed in the upper complex halfplane of energy.

$$G(i\epsilon_R,\mathbf{p}) = -\frac{i\epsilon_R + \boldsymbol{\sigma}\mathbf{p}}{\epsilon_R^2 + p^2}, \quad G(-i\epsilon_A,\mathbf{p}) = \frac{i\epsilon_A - \boldsymbol{\sigma}\mathbf{p}}{\epsilon_A^2 + p^2}, \qquad \epsilon_{R/A} \mapsto \mp iE + 0. \tag{2.5}$$

When only retarded Green functions are used (e.g. in the calculation of the density of states) we will omit the index and write simply ϵ instead of ϵ_R since it obeys the usual convention for Matsubara energy.

Calculating diagrams for a system with linear dispersion in 3D leads to strong ultraviolet divergences. In fact, the theory is free of such problems only in the dimension $d < 2$. To overcome this difficulty, we will use dimensional regularization scheme [42, 45]. This

means calculating every diagram in an arbitrary dimension d and then performing analytic continuation of the result in the parameter d from the domain of convergence $d < 2$ to the point $d = 3$. Ultraviolet divergence, that occurs in most diagrams at $d = 2$, manifests itself as a pole in the corresponding expression as a function of d. Analytic continuation allows to bypass the pole and get some finite result for $d > 2$. We will comment on the physical meaning of this mathematical trick later. Let us stress once again, that unlike numerous other works we do not imply any kind of expansion in the vicinity of the critical dimension $d = 2$ but rather allow for arbitrary values of d.

Three-dimensional momentum integrals are generalized to arbitrary d as

$$\int \frac{d^3p}{(2\pi)^3} \dots \mapsto \int \frac{d^dp}{(2\pi)^d} \dots = \int \frac{S_{d-1}p^{d-1}\,dp}{(2\pi)^d} \dots, \qquad S_{d-1} = \frac{2\pi^{d/2}}{\Gamma(d/2)}. \tag{2.6}$$

Here S_{d-1} is the volume of a $(d-1)$-dimensional unit sphere. The matrix-valued vector $\boldsymbol{\sigma}$ is generalized to d dimensions by imposing anticommutation relations on its elements:

$$\sigma_a\sigma_b + \sigma_b\sigma_a = 2\delta_{ab}, \qquad \delta_{aa} = d, \qquad \operatorname{tr} 1 = 2. \tag{2.7}$$

It might seem weird since no explicit matrix representation exists for σ_a in an arbitrary dimension and the index a itself takes a fractional (or even complex!) number of distinct values. Nevertheless, relations (2.7) are sufficient to calculate any given diagram without resorting to explicit representations of σ matrices. Strictly speaking, the convention $\operatorname{tr} 1 = 2$ does not hold for arbitrary d. For example in $d = 4$, a minimal representation of the Dirac γ matrices has the size 4. However, we will apply dimensional scheme at $d = 3$ where standard Pauli matrices have dimension 2. Hence, for our purposes, the relation $\operatorname{tr} 1 = 2$ is valid.

For the sake of convenience, we also generalize the disorder correlation function (2.2) to arbitrary dimension as follows:

$$\big\langle V(\mathbf{r})V(\mathbf{r}')\big\rangle = \frac{(2\pi)^d}{S_{d-1}}\alpha\,\delta(\mathbf{r}-\mathbf{r}'). \tag{2.8}$$

The parameter α itself has a dimension that depends on d: $[\alpha] = E^{2-d}$.

Our main goal is to calculate average density of states ρ and conductivity σ in the limit of small energy or, equivalently, weak disorder, cf. Eq. (2.3). We will use standard Kubo expressions for these quantities. Density of states is given by a single average Green function at coincident points:

$$\rho(E) = -\frac{1}{\pi}\operatorname{Im}\int \frac{d^dp}{(2\pi)^d}\operatorname{tr}\big\langle G^R(E,\mathbf{p})\big\rangle. \tag{2.9}$$

For a clean system, it is easy to calculate the density of states just by the area of the Fermi surface. In 3D, this yields

$$\rho_0(E) = \frac{4\pi E^2}{(2\pi)^3} = \frac{E^2}{2\pi^2}. \tag{2.10}$$

The same result follows from Eq. (2.9) with the Green function from Eq. (2.4).

Kubo formula for conductivity is

$$\sigma(E) = -\frac{1}{4\pi}\operatorname{Tr}\Big\langle j_x\left[G_R(E) - G_A(E)\right] j_x\left[G_R(E) - G_A(E)\right]\Big\rangle. \tag{2.11}$$

Here 'Tr' implies the trace operator acting on Pauli matrices and also an integral in the momentum space. Current operators are related to the electron velocity

$$\mathbf{j} = e\,\frac{\partial H_0}{\partial \mathbf{p}} = e\boldsymbol{\sigma}. \tag{2.12}$$

If one expands the brackets in Eq. (2.11), there are in total three different terms with products of different types of Green functions. Each individual term contains a formally divergent momentum integral in 3D hidden in the 'Tr' notation. But the integral of all the terms combined in Eq. (2.11) converges. It seems that this property prevents us from discarding the terms with the products $G^R G^R$ and $G^A G^A$. But here we can use one important advantage of the dimensional scheme. Namely, if we consider dimensions $d < 2$, the momentum integral of each individual term becomes convergent. Moreover, the integrals involving two similar Green functions vanish due to gauge invariance [their integrands can be rewritten in terms of a total vector divergence $\mathrm{div}_{\mathbf{p}}\langle \mathbf{j}\, G^{R/A}(\mathbf{p})\rangle$ in the momentum space]. Hence we can simply discard the terms with the products of similar Green functions if, at the same time, we treat the remaining divergent integral as its analytic continuation from $d < 2$. With this convention, we can use the following simplified Kubo formula for conductivity:

$$\sigma(E) = \frac{1}{2\pi}\,\mathrm{Tr}\Big\langle j_x\, G_R(E)\, j_x\, G_A(E)\Big\rangle. \tag{2.13}$$

In the following chapters we will develop a diagrammatic expansion of $\rho(E)$ and $\sigma(E)$ in the small parameter αE based on Eqs. (2.9) and (2.13)

3 Self-consistent Born approximation

A standard approach in the theory of weakly disordered metals is the self-consistent Born approximation (SCBA). It takes into account only the diagrams with non-intersecting impurity lines. Such diagrams are most important because all the Green functions can be taken close to the mass shell (Fermi surface) without violating conservation of momentum. Other diagrams, with intersection of impurity lines acquire an extra small factor in the limit $E\tau \gg 1$. To estimate the disorder scattering rate in our model, we can apply the Fermi golden rule $1/\tau \sim \alpha\rho(E)$. With the density of states (2.10), this yields

$$E\tau \sim \frac{1}{\alpha E} \gg 1. \tag{3.1}$$

Hence the criterion of weak disorder (2.3) also implies validity of SCBA. Let us stress quite a counterintuitive feature of the Weyl semimetal model: disorder effects get weaker with lowering the energy and shrinking of the Fermi surface. For most other common Hamiltonians the situation is opposite: parameter $E\tau$ grows with increasing energy. Weyl semimetals are special in this respect because their density of states has a relatively strong energy dependence with a soft gap at $E = 0$.

In the framework of SCBA, the electron Green function averaged over disorder realizations acquires a self energy which is independent of momentum

$$G(i\epsilon, \mathbf{p}) = \frac{1}{i\epsilon - \boldsymbol{\sigma}\mathbf{p} - \Sigma(i\epsilon)}. \tag{3.2}$$

The self energy $\Sigma(i\epsilon)$ can be found from the self-consistency equation shown diagrammatically in Fig. 3.1. The diagram in the right-hand side of the equation involves the Green function (3.2) that includes the same self energy as in the left-hand side. This self-consistency equation automatically takes into account all the diagrams with non-intersecting impurity lines. Explicitly, the equation is

$$\Sigma = \frac{(2\pi)^d}{S_{d-1}}\,\alpha \int (d^d p)\, G(i\epsilon, \mathbf{p}) = \alpha \int_0^\infty \frac{(i\epsilon - \Sigma)\, p^{d-1}\, dp}{(i\epsilon - \Sigma)^2 - p^2} = -\frac{i\pi\alpha(\epsilon + i\Sigma)^{d-1}}{2\sin(\pi d/2)}. \tag{3.3}$$

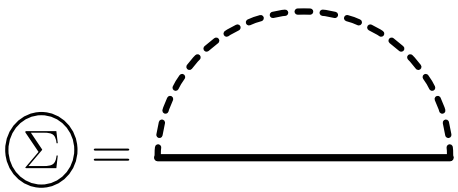

Figure 3.1: SCBA equation (3.3) in the diagrammatic representation. Dashed line represents the disorder correlator (2.8). Solid straight line is the disorder-averaged Green function (3.2) which includes the same self energy Σ as in the left-hand side of the equation.

While the momentum integral here converges only for $d < 2$, we can perform analytic continuation of the result directly to the point $d = 3$. This way we arrive at a simple quadratic equation for the self energy that can be readily solved:

$$\Sigma = \frac{i\pi\alpha}{2}(\epsilon + i\Sigma)^2 = i\epsilon + \frac{i}{\pi\alpha}\Big(1 - \sqrt{1 + 2\pi\alpha\epsilon}\Big). \tag{3.4}$$

This equation and its solution can be directly compared to a similar SCBA equation studied in Ref. [23]. In that work, the divergence of the integral (3.3) was regulated by limiting the momenta $0 < p < \Delta$. As a result, the right-hand side of the equation acquired an extra contribution $\propto \Delta$. However, this extra term only slightly modifies the solution in the limit of weak disorder. Moreover, it can be absorbed into a redefinition of the parameter α and does not show up in the observable quantities.

After analytic continuation of Eq. (3.4) in the upper complex half-plane $i\epsilon \mapsto E + i0$, we obtain the retarded self energy

$$\Sigma^R = E + \frac{\sqrt{1 - 2i\pi\alpha E} - 1}{i\pi\alpha} \approx -\frac{i\pi\alpha E^2}{2} + \frac{\pi^2\alpha^2 E^3}{2} + \dots \tag{3.5}$$

The real part of the self energy can be always hidden in the renormalization of the Fermi energy. In turn, the imaginary part is directly observable since it defines the electron scattering rate

$$\gamma = \frac{1}{2\tau} = -\operatorname{Im}\Sigma^R \approx \frac{\pi\alpha E^2}{2}. \tag{3.6}$$

We see that our SCBA approach within dimensional regularization scheme correctly reproduces the leading Fermi golden rule estimate of this rate, cf. Eq. (3.1).

3.1 Density of states

Average density of states in the presence of disorder is given by Eq. (2.9). This equation contains exactly the same momentum integral as in the right-hand side of the SCBA equation (3.3). This allows us to express the density of states via the self energy directly in 3D:

$$\rho(E) = -\frac{2}{\pi}\operatorname{Im}\int (d^3p)\,\frac{E - \Sigma^R}{(E - \Sigma^R)^2 - p^2} = -\frac{\operatorname{Im}\Sigma^R}{\pi^3\alpha}. \tag{3.7}$$

Using the solution (3.4), we obtain a rather simple and closed expression for the density of states

$$\rho(E) = \frac{\operatorname{Re}\sqrt{1 + 2i\pi\alpha E} - 1}{\pi^4\alpha^2} \approx \frac{E^2}{2\pi^2}\left(1 - \frac{5}{4}\,\pi^2\alpha^2E^2 + \dots\right). \tag{3.8}$$

In the limit of weak disorder, the density of states acquires a small negative correction $\propto \alpha^2E^2$. In the next chapter we will show that other diagrams, not included in SCBA, provide a stronger correction in this limit. Let us also point out that the SCBA result for the density of states is an analytic function at small E. Corrections beyond SCBA will violate this property as well.

3.2 Conductivity

Semiclassical conductivity is defined by the Kubo formula (2.13) with the two Green functions averaged separately. In addition, the current vertex correction shown in Fig. 3.2 should

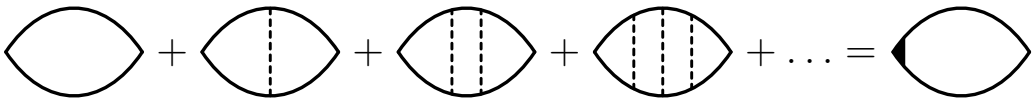

Figure 3.2: Diagrams for conductivity with the current vertex correction.

be included in order to account for all the diagrams with non-intersecting impurity lines. As we will see shortly, each rung of the ladder diagram multiplies the current operator by the same constant W:

$$W j_x = \alpha \int G^R(i\epsilon_R, \mathbf{p}) j_x G^A(-i\epsilon_A, \mathbf{p})\, p^{d-1}\, dp = e\alpha \int \frac{\epsilon_R \sigma_x \epsilon_A + (\boldsymbol{\sigma}\mathbf{p})\sigma_x(\boldsymbol{\sigma}\mathbf{p})}{(\epsilon_R^2 + p^2)(\epsilon_A^2 + p^2)}\, p^{d-1}\, dp. \quad (3.9)$$

Here we use Matsubara representation with both energies $\epsilon_{R/A}$ positive, cf. Eq. (2.5). These energies also include the corresponding self-energy parts.

Averaging over directions of $\mathbf{p}$ and applying anticommutation rules (2.7), we simplify the second term in the numerator of Eq. (3.9):

$$(\boldsymbol{\sigma}\mathbf{p})\sigma_x(\boldsymbol{\sigma}\mathbf{p}) \mapsto \frac{p^2}{d}\, \sigma_a \sigma_x \sigma_a = \frac{2-d}{d}\, p^2 \sigma_x. \quad (3.10)$$

This way we prove that the right-hand side of Eq. (3.9) is indeed proportional to σ_x and hence the current operator retains its matrix form.

The remaining integral over p, that defines the factor W, can be split into two parts with either retarded or advanced denominator:

$$\begin{aligned} W &= \alpha \int \frac{\epsilon_R \epsilon_A + p^2(2-d)/d}{(\epsilon_R^2 + p^2)(\epsilon_A^2 + p^2)}\, p^{d-1}\, dp \\ &= \frac{\alpha}{d(\epsilon_R^2 - \epsilon_A^2)} \int \left(\frac{\epsilon_A[d\epsilon_R + (d-2)\epsilon_A]}{\epsilon_A^2 + p^2} - \frac{\epsilon_R[(d-2)\epsilon_R + d\epsilon_A]}{\epsilon_R^2 + p^2} \right) p^{d-1}\, dp. \end{aligned} \quad (3.11)$$

This separation allows us to express the integrals of the two terms through the self energy using the SCBA equation (3.3):

$$W = \frac{-i}{d(\epsilon_R^2 - \epsilon_A^2)} \Big(\big[d\epsilon_R + (d-2)\epsilon_A\big]\Sigma^A + \big[(d-2)\epsilon_R + d\epsilon_A\big]\Sigma^R \Big). \quad (3.12)$$

Finally, we perform analytic continuation to real energies according to the rules

$$i\epsilon_R \mapsto E - \Sigma^R, \qquad -i\epsilon_A \mapsto E - \Sigma^A \quad (3.13)$$

and get the following result:

$$W = \frac{E + (d-2)\,\mathrm{Re}\,\Sigma}{d(E - \mathrm{Re}\,\Sigma)}. \quad (3.14)$$

The diagrams in Fig. 3.2 represent a simple geometric series with the denominator W. Summing up this series and setting $d = 3$, we obtain the conductivity

$$\sigma = \frac{e^2}{2\pi^3 \alpha} \frac{W}{1-W} = \frac{e^2}{4\pi^3 \alpha} \frac{E + \mathrm{Re}\,\Sigma}{E - 2\,\mathrm{Re}\,\Sigma}. \quad (3.15)$$

With the solution (3.5), we can get a closed expression for the conductivity including all diagrams with non-intersecting impurity lines.

$$\sigma = \frac{e^2}{4\pi^3 \alpha} \frac{1 - 2\,\mathrm{Re}\sqrt{1 + 2i\pi\alpha E}}{\mathrm{Re}\sqrt{1 + 2i\pi\alpha E} - 2} \approx \frac{e^2}{4\pi^3 \alpha} \left(1 + \frac{3}{2}\, \pi^2 \alpha^2 E^2 + \dots \right). \quad (3.16)$$

Exactly at the Weyl point, $E = 0$, the conductivity remains finite. Its value is $\propto 1/\alpha$. This result fully agrees with the previous studies [22, 23]. Equation (3.16) suggests a correction $\propto E^2$ to this constant. In the next chapter, we will show that other diagrams, not included in SCBA, provide a stronger correction, that is also non-analytic at small energies.

4 Interference corrections

In the previous chapter, we have calculated the average density of states and conductivity of a Weyl semimetal using self-consistent Born approximation. This approach automatically includes the complete set of diagrams with non-intersecting impurity lines. In a sense, it is a mean-field approach neglecting possible interference of electrons scattering on different impurities. We will now take into account such interference effects and consider diagrams with crossed impurity lines.

The most prominent effect based on quantum interference of electrons is Anderson localization [46]. It has numerous forms depending on the symmetry of disordered Hamiltonian, on certain topological features of the spectrum, and on the system dimensionality. For the case of 3D Weyl semimetals, as for any other 3D material, localization effects are weak unless disorder strength exceeds a certain threshold value. This weak localization correction in 3D is $\delta\sigma \sim e^2/l$, where l is the electron's mean free path. Using Eq. (3.6), we can estimate the weak localization correction in our model as $\delta\sigma \sim e^2\alpha E^2$. Such a correction is the result of summation of an infinite set of maximally crossed diagrams [47]. Quite curiously, weak localization effect is of the same order as the correction to conductivity due to non-intersecting diagrams (3.16). In this chapter we will calculate crossed diagrams with two and three impurity lines. It will be shown that these diagrams provide a stronger interference correction than the weak localization effect.

Our calculation is technically similar to the treatment of ballistic interference effects in a conventional disordered metal with parabolic dispersion. Such a calculation was carried out in Refs. [43, 44]. However, in the case of Weyl semimetals additional complications arise due to the matrix structure of the Hamiltonian (2.1).

4.1 Density of states

The first non-trivial diagram that provides an interference correction to the density of states (3.8) involves two crossed impurity lines. This diagram is shown in Fig. 4.1. Since all the Green functions in this diagram are taken at the same energy, we can considerably simplify the calculation by computing the corresponding vacuum diagram first and then taking its derivative in energy

$$\delta\rho(E) = -\frac{1}{\pi}\,\mathrm{Im}\,\frac{\partial F_2(E+i0)}{\partial E}, \tag{4.1}$$

$$F_2(i\epsilon) = -\frac{1}{4}\left(\frac{(2\pi)^d\alpha}{S_{d-1}}\right)^2 \int (d^dq)\,\mathrm{tr}\Big[\Pi(i\epsilon,\mathbf{q})\Pi(i\epsilon,-\mathbf{q})\Big], \tag{4.2}$$

$$\Pi(i\epsilon,\mathbf{q}) = \int (d^dp)\,G(i\epsilon,\mathbf{p}+\mathbf{q})G(i\epsilon,-\mathbf{p}). \tag{4.3}$$

Strictly speaking, we should retain the self-energy contribution in the Green functions and take analytic continuation from a Matsubara energy $i\epsilon$ to the energy $E+i\gamma$. However, for

$$\delta\rho(E) = -\frac{1}{\pi}\,\mathrm{Im}$$ 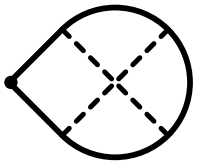 $$= -\frac{1}{\pi}\,\mathrm{Im}\,\frac{\partial}{\partial E}$$ 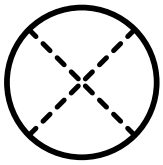

Figure 4.1: Interference correction to the density of states in two equivalent forms: as a Green function at coincident points and as an energy derivative of a vacuum diagram.

the calculation of the density of states, the extra imaginary part of the self energy γ can be neglected since it provides a correction of a higher order in αE.

Four Green functions in the vacuum diagram Fig. 4.1 are split into two similar pairs and the result of momentum integration inside each pair is denoted by Π. Let us first analyze this latter integral of the product of two Green functions.

$$\Pi(i\epsilon,\mathbf{q}) = \int (d^dp)\frac{(i\epsilon+\boldsymbol{\sigma}\mathbf{p}+\boldsymbol{\sigma}\mathbf{q})(i\epsilon+\boldsymbol{\sigma}\mathbf{p})}{[\epsilon^2+(\mathbf{p}+\mathbf{q})^2][\epsilon^2+p^2]} = \int (d^dp)\frac{-\epsilon^2+i\epsilon\boldsymbol{\sigma}(2\mathbf{p}+\mathbf{q})+p^2+(\boldsymbol{\sigma}\mathbf{p})(\boldsymbol{\sigma}\mathbf{q})}{[\epsilon^2+(\mathbf{p}+\mathbf{q})^2][\epsilon^2+p^2]}. \tag{4.4}$$

At this stage, we will average over directions of the momentum $\mathbf{p}$. We separate a component of $\mathbf{p}$ parallel to $\mathbf{q}$ and a perpendicular component $\mathbf{p}_\perp$:

$$\mathbf{p} = \frac{\mathbf{pq}}{q^2}\,\mathbf{q} + \mathbf{p}_\perp. \tag{4.5}$$

The denominator of the integrand in Eq. (4.4) is independent of the direction of $\mathbf{p}_\perp$. Hence we can average the numerator with respect to this direction. Effectively, it means dropping all the terms which are odd in $\mathbf{p}_\perp$. The result is

$$\Pi(i\epsilon,\mathbf{q}) = \int (d^dp)\frac{-\epsilon^2+p^2+\mathbf{pq}+i\epsilon\boldsymbol{\sigma}\mathbf{q}(1+2\mathbf{pq}/q^2)}{[\epsilon^2+(\mathbf{p}+\mathbf{q})^2][\epsilon^2+p^2]}. \tag{4.6}$$

Next, we replace the scalar product

$$\mathbf{pq} = \frac{(\mathbf{p}+\mathbf{q})^2-p^2-q^2}{2} \tag{4.7}$$

and expand the integrand in separate fractions such that their numerators do not contain $\mathbf{p}$.

$$\Pi(i\epsilon,\mathbf{q}) = \int (d^dp)\left[\frac{-2\epsilon^2-q^2/2}{[\epsilon^2+(\mathbf{p}+\mathbf{q})^2][\epsilon^2+p^2]} + \left(\frac{1}{2}-\frac{i\epsilon\boldsymbol{\sigma}\mathbf{q}}{q^2}\right)\frac{1}{\epsilon^2+(\mathbf{p}+\mathbf{q})^2} + \left(\frac{1}{2}+\frac{i\epsilon\boldsymbol{\sigma}\mathbf{q}}{q^2}\right)\frac{1}{\epsilon^2+p^2}\right]. \tag{4.8}$$

Finally, we shift the variable in the second term $\mathbf{p}+\mathbf{q}\mapsto\mathbf{p}$ and combine it with the last term of the integrand. This way we represented Π as a combination of two basic integrals:

$$I(i\epsilon) = \int \frac{p^{d-1}\,dp}{\epsilon^2+p^2} = \frac{\pi\epsilon^{d-2}}{2\sin(\pi d/2)}, \qquad I(i\epsilon,i\epsilon,q) = \int \frac{p^{d-1}\,dp}{[\epsilon^2+(\mathbf{p}+\mathbf{q})^2][\epsilon^2+p^2]}. \tag{4.9}$$

The first of these integrals we have already encountered earlier in the calculation of the self energy (3.3). The second integral is more complicated since its denominator has a nontrivial

dependence on the angle between $\mathbf{p}$ and $\mathbf{q}$. This latter integral is in fact similar to the polarization operator for a Hamiltonian with quadratic dispersion. Calculation of such a polarization operator and its analytic continuation to real energies is analyzed in detail in Appendix A. The final result for Π is

$$\Pi(i\epsilon, \mathbf{q}) = I(i\epsilon) - \left(2\epsilon^2 + \frac{q^2}{2}\right) I(i\epsilon, i\epsilon, q). \tag{4.10}$$

Once the value of Π is known, we can readily use Eq. (4.2) and represent the vacuum diagram as a single integral in q. At the same time, we perform analytic continuation to real energies and obtain

$$F_2(E + i0) = -\frac{\alpha^2}{2} \int (d^d q) \left[I_R + \left(2E^2 - \frac{q^2}{2}\right) I_{RR}(q) \right]^2. \tag{4.11}$$

Here I_R is the retarded form of the first integral in Eq. (4.9) and I_{RR} is the retarded-retarded form of the polarization operator (A.6).

Integral (4.11) diverges at large q in 3D. We can extract this divergent part by using the simplified form of the polarization operator (A.8b) and expanding in $q \gg E$:

$$F_2(E + i0) = \text{const} - \alpha^2 \int_E^\infty dq \left[\frac{\pi^2}{256}\, q^{3d-9} (q^2 - 4E^2)^2 - \frac{i\pi}{60}\, E^d q^{2d-7} (5q^2 - 16E^2) \right]. \tag{4.12}$$

Lower bound of the integral is set to E since this is effectively the only available parameter of the proper dimension. The exact value of this lower bound is immaterial since we can always change it at the cost of redefining the constant term.

Dimensional regularization implies that the divergent integral in Eq. (4.12) is calculated assuming d is low enough ($d < 4/3$ in this case) and then the result is analytically continued to $d = 3$. Strongly divergent terms provide some finite contributions after this procedure. This is fully analogous to how the divergent real part of the self energy is removed by renormalization of the chemical potential. The only non-trivial contribution comes from the very last term whose divergence in 3D is logarithmic.

$$F_2(E + i0) = \text{const} - \frac{4i\pi\alpha^2}{15}\, E^{d+2} \int_E^\infty dq\, q^{2d-7} = \text{const} + \frac{2i\pi\alpha^2}{15}\, \frac{E^{3d-4}}{d-3}. \tag{4.13}$$

Thus, the function F_2 acquires a simple pole at $d = 3$. This is a standard manifestation of a logarithmic divergence in dimensional scheme. We can convert this pole into explicit logarithm by expanding the numerator near $d = 3$:

$$F_2(E + i0) = \frac{2i\pi}{15}\, \alpha^2 E^5 \left(\frac{1}{d-3} + 3 \ln E + \dots \right) = \frac{2i\pi}{5}\, \alpha^2 E^5 \ln |E/\Delta|. \tag{4.14}$$

The divergent term $1/(d-3)$ should be replaced by some large number related to the ultraviolet cutoff scale Δ. We simply incorporate this scale into the logarithmic factor as shown in the last expression.

Interference correction to the average density of states can be found from Eq. (4.1). Together with the SCBA expression (3.8), this gives the final result

$$\rho(E) = \frac{E^2}{2\pi^2} - 2\alpha^2 E^4 \ln |E/\Delta| + O(\alpha^2 E^4). \tag{4.15}$$

Remarkably, interference correction to the density of states is stronger than a similar correction from SCBA due to just an extra logarithm factor. At the same time, this logarithmic correction is non-analytic as a function of energy in the limit $E \to 0$ unlike the SCBA result.

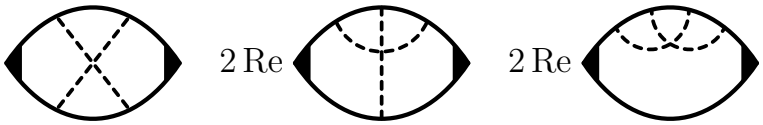

Figure 4.2: Interference corrections to conductivity with two crossed impurity lines.

4.2 Conductivity

Let us now consider similar interference corrections to the quasiclassical conductivity (3.16). The calculation will be carried out exactly with the same strategy as we did for the density of states. First, we will reduce every diagram to a single d-dimensional integral over momentum q in terms of polarization operators. Then we will expand the integrand in small ratio γ/E and retain only relevant leading terms of this expansion. Finally, we will analyse ultraviolet behavior of each term and apply dimensional scheme to treat divergent contributions.

4.2.1 Diagrams with two crossed impurity lines

There are in total three different interference diagrams for conductivity with two crossed impurity lines, see Fig. 4.2. All these diagrams can be generated from the single vacuum diagram Fig. 4.1 by inserting two current vertices in different positions. However, unlike the case of the density of states, we cannot calculate conductivity by taking derivatives of the vacuum diagram in some parameter because the conductivity diagram involves both retarded and advanced Green functions.

Consider the first diagram, Fig. 4.2a. We can write it explicitly as

$$\delta\sigma_a^{(2)} = \frac{e^2\alpha^2}{2\pi(1-W)^2}\int (d^dq)\, p_1^{d-1}\, dp_1\, p_2^{d-1}\, dp_2\, \mathrm{tr}\Big[\sigma_x G^R(\mathbf{p}_1+\mathbf{q})G^R(\mathbf{p}_2+\mathbf{q})G^R(-\mathbf{p}_1) \times \sigma_x G^A(-\mathbf{p}_1)G^A(-\mathbf{p}_2)G^A(\mathbf{p}_1+\mathbf{q})\Big]. \quad (4.16)$$

Here we have already included two vertex corrections (3.14).

Our first goal is to reduce the integrand to a product of polarization operators. Each polarization operator will incorporate integration over p_1 or p_2 and the q integral will be analyzed later. However, our expression contains four Green functions which involve momentum p_1. Therefore we reduce the denominators by applying the identity

$$\frac{1}{(\epsilon_R^2+p^2)(\epsilon_A^2+p^2)} = \frac{1}{\epsilon_A^2-\epsilon_R^2}\left(\frac{1}{\epsilon_R^2+p^2}-\frac{1}{\epsilon_A^2+p^2}\right) \quad (4.17)$$

twice. This is fully analogous to the splitting of denominators in Eq. (3.11).

The next step is taking the trace of σ matrices in the numerator and averaging over directions of $\mathbf{p}_{1,2}$ as was explained earlier in the calculation of the density of states. Finally, we apply Eq. (4.7) to the momenta $\mathbf{p}_{1,2}$ and split the integrand in individual fractions whose numerators are independent of $\mathbf{p}_{1,2}$. This way we represent $\delta\sigma_a^{(2)}$ as a single q integral of a quadratic expression in terms of polarization operators.

$$\delta\sigma_a^{(2)} = \int_0^\infty dq\, S_a(q). \quad (4.18)$$

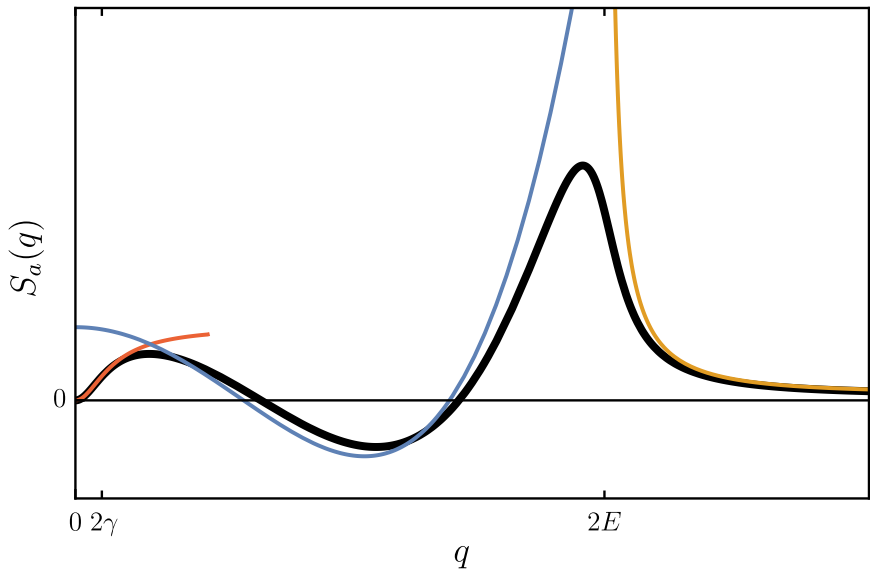

Figure 4.3: Momentum dependence of the integrand $S_a(q)$ for the representation (4.18) of the diagram Fig. 4.2a (thick black curve). Parameters of the plot $\gamma/E = 0.05$. Three asymptotic expressions Eqs. (4.19), (4.20) are shown by the red, blue, and orange lines, respectively.

Explicit form of the function $S_a^{(2)}(q)$ for an arbitrary d is very cumbersome hence we only show the integrand graphically in Fig. 4.3 for the case $d = 3$. There are three qualitatively different regions in this function:

$$S_a(q) = \begin{cases} S_a^{\mathrm{I}}(q), & q \lesssim \gamma, \\ S_a^{\mathrm{II}}(q), & \gamma \ll q < 2E, \\ S_a^{\mathrm{III}}(q), & q > 2E. \end{cases} \tag{4.19}$$

To analyse the integral, we can do further simplifications by setting $d = 3$ in the first two regions and by expanding to the leading orders in the small parameter γ/E. This way we obtain the following expressions:

$$S_a^{\mathrm{I}}(q) = -\frac{3e^2}{16\pi^3}\left[\frac{2\gamma}{q} - \left(1 + \frac{4\gamma^2}{q^2}\right)\arctan\frac{q}{2\gamma}\right]\left[\frac{6\gamma}{q} + \left(1 - \frac{12\gamma^2}{q^2}\right)\arctan\frac{q}{2\gamma}\right], \tag{4.20a}$$

$$S_a^{\mathrm{II}}(q) = \frac{9e^2}{64\pi}\left(\frac{1}{3} - \frac{q^2}{E^2} + \frac{7q^4}{16E^4} - \frac{q^6}{96E^6}\right), \tag{4.20b}$$

$$S_a^{\mathrm{III}}(q) = \frac{3e^2\alpha}{64\pi}\, q^{2d-5}\left[15 - \frac{q^2}{2E^2} - \frac{16E^2}{4E^2 - q^2} + \left(\frac{q^3}{4E^3} - \frac{15q}{2E} + \frac{2E}{q}\right)\operatorname{arctanh}\frac{2E}{q}\right]. \tag{4.20c}$$

These three asymptotic forms are also illustrated in Fig. 4.3. Let us remind that parameters γ and α are related by Eq. (3.6) in 3D. For $d \approx 3$, a slightly more general relation

$$\gamma = \frac{\pi}{2}\,\alpha E^{d-1}. \tag{4.21}$$

is used.

The first asymptotic region $q \lesssim \gamma$ provides a contribution to the conductivity $\propto \alpha E^2$. This part is normally taken into account in the weak localization correction. We will neglect

it in favor of other, larger contributions. Integral over the second region $\gamma \ll q < 2E$ converges and provides a correction

$$\int_0^{2E} dq\, S_a^{\rm II}(q) = \frac{3e^2|E|}{35\pi}. \tag{4.22}$$

This correction is smaller than the leading Drude result (3.16) but, at the same time, larger than both weak localization and the subleading term in Eq. (3.16). Remarkably, unlike the SCBA result, this term is of an odd power in E and hence exhibits a cusp at $E = 0$. We stress this fact by writing explicitly the absolute value $|E|$ in Eq. (4.22) thus allowing for E of any sign.

Contribution of the third asymptotic region $q > 2E$ has an extra α factor compared to $S_a^{\rm II}$ hence it should be negligible at first sight. However, it contains an ultraviolet divergence that can lead to an extra logarithmic factor as we have already seen in the calculation of the density of states. To analyse ultraviolet behavior, we expand $S_a^{\rm III}(q)$ in the limit $q \gg E$ and keep divergent terms only.

$$\begin{aligned}\int_{2E}^{\infty} dq\, S_a^{\rm III}(q) &= \text{const} + e^2\alpha \int_{2E}^{\infty} dq \left(\frac{q^{2d-5}}{32\pi} + \frac{3E^2 q^{2d-7}}{40\pi} \right) \\ &= \text{const} - \frac{3e^2\alpha E^{2d-4}}{80\pi(d-3)} = \text{const} - \frac{3e^2}{40\pi}\,\alpha E^2 \ln|E/\Delta|. \end{aligned} \tag{4.23}$$

We conclude that the contribution of this part, although having an extra αE factor as compared to Eq. (4.22), is still dominant compared to both the weak localization and the SCBA subleading term (3.16) due to an extra logarithm. Collecting all the terms together, we have the following result for the diagram Fig. 4.2a:

$$\delta\sigma_a^{(2)} = \frac{3e^2|E|}{35\pi} - \frac{3e^2}{40\pi}\,\alpha E^2 \ln|E/\Delta|. \tag{4.24a}$$

Calculation of the other two diagrams in Fig. 4.2 is performed in exactly the same way. The only slight technical difference for the diagram Fig. 4.2c is the presence of two identical Green functions. This means that in some terms we will encounter a square of the Green function's denominator. These terms should be expressed via an energy derivative of the polarization operator. The results for the two diagrams are

$$\delta\sigma_b^{(2)} = \frac{3e^2}{20\pi}\,\alpha E^2 \ln|E/\Delta|, \tag{4.24b}$$

$$\delta\sigma_c^{(2)} = -\frac{e^2|E|}{5\pi} + \frac{e^2}{8\pi}\,\alpha E^2 \ln|E/\Delta|. \tag{4.24c}$$

Overall interference correction to the conductivity from diagrams Fig. 4.2 is the sum of Eqs. (4.24):

$$\delta\sigma^{(2)} = -\frac{4e^2|E|}{35\pi} + \frac{e^2}{5\pi}\,\alpha E^2 \ln|E/\Delta|. \tag{4.25}$$

This result contains both the leading ($\propto \alpha^0$) and the subleading ($\propto \alpha^1$) terms. Higher diagrams with three crossed lines have an extra α factor and can provide additional contributions to the subleading interference correction. These diagrams will be studied in the next section.

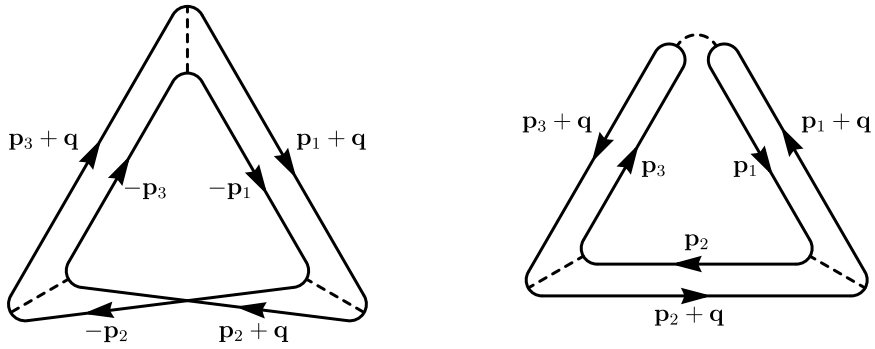

Figure 4.4: Two-particle irreducible vacuum diagrams with three impurity lines. Momentum labels (and triangular shape) show the separation into three polarization operators each involving an integral over $\mathbf{p}_{1,2,3}$.

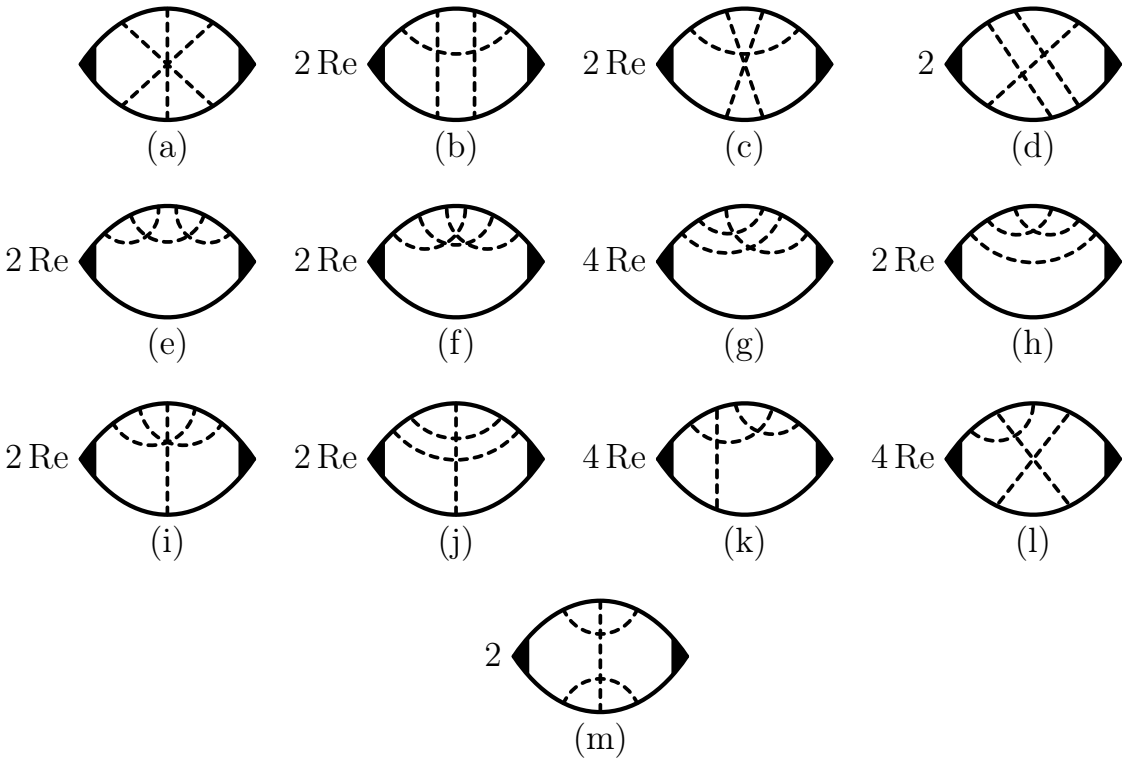

Figure 4.5: Interference corrections to the conductivity with three crossed impurity lines.

4.2.2 Diagrams with three crossed impurity lines

In this section we study interference diagrams for conductivity with three crossed impurity lines. All such diagrams (except one, see below) can be generated from just two distinct vacuum diagrams by inserting two current vertices in all possible positions. The relevant vacuum diagrams are shown in Fig. 4.4. Each of the two diagrams can be represented as an integral over single momentum q of a product of three polarization operators, see momentum labels in Fig. 4.4. This property is preserved after insertion of current vertices since they can only double certain denominators, that are later decoupled by the identity (4.17).

The full list of three-impurity diagrams is shown in Fig. 4.5. There is one special diagram (h) in this list which is not generated from the vacuum diagrams of Fig. 4.4. We will consider this diagram separately in the end. All other diagrams are calculated with the same method

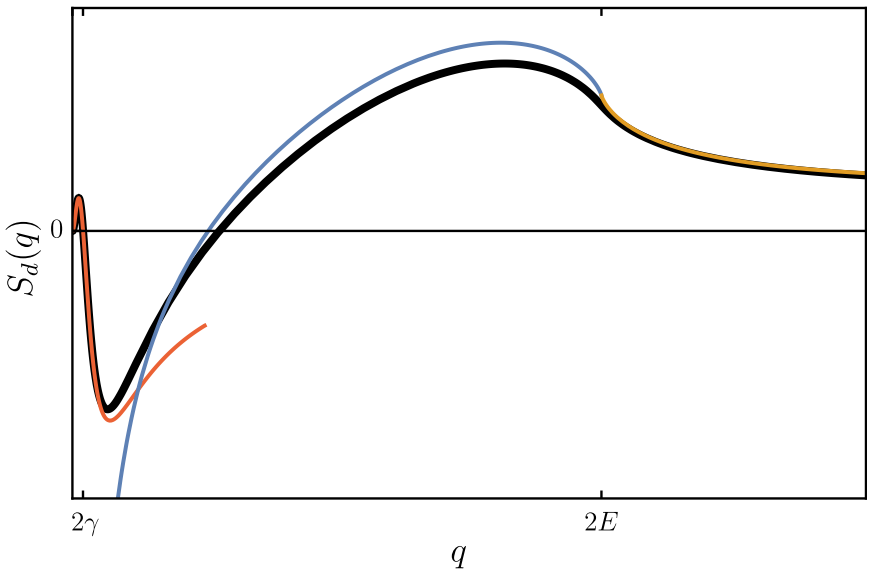

Figure 4.6: Momentum dependence of the integrand $S_d(q)$ for the representation (4.26) of the diagram Fig. 4.5d (thick black curve). Parameters of the plot $\gamma/E = 0.02$. Three asymptotic expressions (4.27) are shown by the red, blue, and orange lines.

as was described in the previous section for diagrams with two impurities. As a typical example, we will explain the calculation of the diagram Fig. 4.5d and then give the results for all other diagrams.

The diagram Fig. 4.5d can be written as a momentum integral of up to three polarization operators (A.8) after taking the trace of all the Green functions, averaging over directions of momenta $\mathbf{p}_{1,2,3}$, and algebraically splitting into individual fractions whose numerators are independent of $\mathbf{p}_{1,2,3}$. All these steps are completely analogous to the calculation of the two-impurity diagrams in the previous section. After extensive algebra, we arrive at the single q integral

$$\delta\sigma_d^{(3)} = \int_0^\infty dq\, S_d(q). \tag{4.26}$$

The integrand of this expression is shown in Fig. 4.6. We can again approximate it in three asymptotic regions of small, intermediate, and large q:

$$S_d(q) = \begin{cases} S_d^{\mathrm{I}}(q), & q \lesssim \gamma, \\ S_d^{\mathrm{II}}(q), & \gamma \ll q < 2E, \\ S_d^{\mathrm{III}}(q), & q > 2E. \end{cases} \tag{4.27}$$

These asymptotic forms are calculated in the same way as we did it earlier for the two-impurity diagram. They are also shown in Fig. 4.6, however, explicit asymptotic expressions are still too bulky to write them here.

The first region provides a finite correction of the order αE^2 completely similar to the previously studied case of two impurities. We will disregard this contribution altogether. In the second region we now have one extra α factor in comparison to the diagram with two impurities. Hence it seems that we can neglect the contribution from this region as well. However, as can be seen from Fig. 4.6, this intermediate region develops a new type of

divergence towards lower values of q. Specifically, we can extract the following asymptotics:

$$S_d(\gamma \ll q \ll E) = S_d^{\rm II}(q \ll E) = -\frac{3(16-\pi^2)}{128\pi}\,\frac{e^2\alpha E^2}{q}. \tag{4.28}$$

Integral of this term is not truly divergent since it is limited by γ from below. But it does provide a logarithmic correction:

$$\int_0^{2E} dq\, S_d(q) = \text{const} + \frac{3(16-\pi^2)}{128\pi}\, e^2\alpha E^2 \ln|\alpha E|. \tag{4.29}$$

The constant term here is of the order αE^2 without any logarithm.

Finally, we can evaluate the contribution of the region $q > 2E$. Full asymptotic expression $S_d^{\rm III}$ is also not needed for this calculation. It suffices to take only divergent terms in the limit $q \to \infty$ and apply the dimensional regularization recipe.

$$\begin{aligned}\int_{2E}^{\infty} dq\, S_d(q) &= \text{const} + e^2\alpha \int_{2E}^{\infty} dq \left(\frac{q^{2d-5}}{48\pi} + \frac{23E^2 q^{2d-7}}{120\pi}\right) \\ &= \text{const} - \frac{23e^2\alpha E^{2d-4}}{240\pi(d-3)} = \text{const} - \frac{23e^2}{120\pi}\,\alpha E^2 \ln|E/\Delta|. \end{aligned} \tag{4.30}$$

Full contribution of the diagram Fig. 4.5d is thus

$$\delta\sigma_d^{(3)} = \frac{e^2}{\pi}\,\alpha E^2 \left[\frac{3}{128}\,(16-\pi^2)\ln|\alpha E| - \frac{23}{120}\,\ln|E/\Delta|\right]. \tag{4.31d}$$

All other diagrams of Fig. 4.5 except (h) are evaluated in the same way and the results are

$$\delta\sigma_a^{(3)} = \frac{e^2}{\pi}\,\alpha E^2 \left[\frac{3}{256}\,(16-3\pi^2)\ln|\alpha E|\right], \tag{4.31a}$$

$$\delta\sigma_b^{(3)} = \frac{e^2}{\pi}\,\alpha E^2 \left[\frac{3}{128}\,(\pi^2-16)\ln|\alpha E| - \frac{41}{120}\,\ln|E/\Delta|\right], \tag{4.31b}$$

$$\delta\sigma_c^{(3)} = \frac{e^2}{\pi}\,\alpha E^2 \left[\frac{1}{768}\,(9\pi^2+16)\ln|\alpha E| + \frac{1}{120}\,\ln|E/\Delta|\right], \tag{4.31c}$$

$$\delta\sigma_e^{(3)} = \frac{e^2}{\pi}\,\alpha E^2 \left[-\frac{1}{3}\,\ln|E/\Delta|\right], \tag{4.31e}$$

$$\delta\sigma_f^{(3)} = \frac{e^2}{\pi}\,\alpha E^2 \left[\frac{47}{24}\,\ln|E/\Delta|\right], \tag{4.31f}$$

$$\delta\sigma_g^{(3)} = \frac{e^2}{\pi}\,\alpha E^2 \left[-\frac{2}{3}\,\ln|E/\Delta|\right], \tag{4.31g}$$

$$\delta\sigma_i^{(3)} = \frac{e^2}{\pi}\,\alpha E^2 \left[-\frac{7}{24}\,\ln|E/\Delta|\right], \tag{4.31i}$$

$$\delta\sigma_j^{(3)} = 0, \tag{4.31j}$$

$$\delta\sigma_k^{(3)} = \frac{e^2}{\pi}\,\alpha E^2 \left[-\frac{1}{12}\,\ln|E/\Delta|\right], \tag{4.31k}$$

$$\delta\sigma_l^{(3)} = \frac{e^2}{\pi}\,\alpha E^2 \left[\frac{13}{60}\,\ln|E/\Delta|\right], \tag{4.31l}$$

$$\delta\sigma_m^{(3)} = 0. \tag{4.31m}$$

It remains to calculate the last diagram Fig. 4.5h. Not all impurity lines intersect in this diagram hence it decouples into two separate integrals. Consider first the part with two current vertices and three adjacent Green functions.

$$\frac{e^2\alpha}{2\pi(1-W)^2}\int p^{d-1}\,dp\,G^R(\mathbf{p})\sigma_x G^A(\mathbf{p})\sigma_x G^R(\mathbf{p}) \\ = \frac{9e^2\alpha}{8\pi}\int p^{d-1}\,dp\,\frac{i\epsilon_A(p^2-\epsilon_R^2)-2i\epsilon_R p^2(2-d)/d}{(\epsilon_R^2+p^2)^2(\epsilon_A^2+p^2)} = -\frac{3ie^2E^{1-d}}{8\pi^2\alpha}. \quad (4.32)$$

We observe that after $\mathbf{p}$ integration this part of the diagram has a trivial matrix structure and can be taken out of the overall matrix trace. Then, the rest of the diagram with two crossed impurity lines is identical to the diagram Fig. 4.1 for the interference correction to the density of states. Using Eq. (4.13), we obtain the following result for the correction to conductivity:

$$\delta\sigma_h^{(3)} = \frac{3e^2E^{1-d}}{4\pi^2\alpha}\,\mathrm{Im}\,\frac{\partial F_2}{\partial E} = \mathrm{const} + \frac{e^2\alpha E^{2d-4}}{2\pi(d-3)} = \frac{e^2}{\pi}\,\alpha E^2\ln|E/\Delta|. \quad (4.31\mathrm{h})$$

Summing up all three-impurity diagrams, we obtain

$$\delta\sigma^{(3)} = \frac{e^2}{8\pi}\left(\frac{5}{3}-\frac{3\pi^2}{16}\right)\alpha E^2\ln|\alpha E| + \frac{51e^2}{40\pi}\,\alpha E^2\ln|E/\Delta|. \quad (4.33)$$

Together with the SCBA expression (3.16) and with the corrections from diagrams with two impurities (4.25), we have the final result for conductivity

$$\sigma = \frac{e^2}{4\pi^3\alpha} - \frac{4e^2|E|}{35\pi} + \frac{e^2}{8\pi}\left(\frac{5}{3}-\frac{3\pi^2}{16}\right)\alpha E^2\ln|\alpha E| + \frac{59e^2}{40\pi}\,\alpha E^2\ln|E/\Delta| + O(\alpha E^2). \quad (4.34)$$

We have thus established the leading and the subleading terms in the energy dependence of conductivity.

The result (4.34) is written in terms of the disorder strength parameter α and the Fermi energy E. Both these parameters also include some uncontrollable renormalization constants that were implicitly included by the dimensional regularization procedure [e.g. an ultraviolet divergent part of the self energy in Eq. (3.3)]. Neither the Fermi energy nor the disorder strength are observable parameters of the material. At the same time, conductivity can be measured directly as a function of electron concentration. The latter can be also controlled, at least in principle, by chemical doping or external gating.

Electron concentration is related to the Fermi energy by integrating the density of states. For our purpose, it is in fact sufficient to retain just the leading term in Eq. (4.15), which is the density of states of a clean Weyl semimetal (2.10)

$$n(E) = \int_0^E dE\,\rho(E) = \frac{E^3}{6\pi^2}, \qquad E = (6\pi^2 n)^{1/3}. \quad (4.35)$$

We substitute this expression for energy into Eq. (4.34) and find

$$\sigma = \frac{e^2}{\hbar}\left[\sigma_0 + An^{1/3} + \frac{n^{2/3}}{\sigma_0}\left(B\ln|n/\sigma_0^3| + C\ln|n/\Delta^3|\right)\right]. \quad (4.36)$$

We have also introduced here the parameter σ_0 corresponding to the conductivity at zero doping in units $e^2/\hbar$. This parameter is also directly measurable and replaces α. Our result

(4.36) is thus a relation involving only observable quantities. Three constants in this relation are

$$A = -\frac{4 \times 6^{1/3}}{35\pi^{1/3}} \approx -0.1418, \tag{4.37}$$

$$B = \frac{6^{2/3}}{32\pi^{8/3}}\left(\frac{5}{3} - \frac{3\pi^2}{16}\right) \approx -0.0009, \tag{4.38}$$

$$C = \frac{59}{80 \times 6^{1/3}\pi^{8/3}} \approx 0.0192. \tag{4.39}$$

While the electron concentration is at least partially controllable in the experiment, it seems unfeasible that amount of disorder can be changed at will. That is why the two logarithmic terms in Eq. (4.36) can hardly be distinguished. A simplified version of our result with the two logarithms combined reads

$$\sigma = e^2\left[\sigma_0 + An^{1/3} + (B+C)\frac{n^{2/3}}{\sigma_0}\ln|n|\right]. \tag{4.40}$$

Here a normalization constant under the logarithm is unspecified and the prefactor of the second term is $B + C \approx 0.0183$.

5 Summary and discussion

To summarize, we have studied spectral and transport properties of a 3D Weyl semimetal in the presence of Gaussian white-noise disorder. We have developed perturbation theory in the weak disorder limit controlled by the parameter $\alpha E \ll 1$ using dimensional regularization scheme near $d = 3$. Both semiclassical and interference contributions were taken into account to calculate the average density of states and conductivity.

In the framework of the self-consistent Born approximation, we have found a closed analytic expression for the self energy in three dimensions (3.4). This allowed us to derive full mean-field results for the density of states (3.8) and conductivity (3.16) taking into account the whole set of non-intersecting diagrams. Both quantities are analytic functions in the limit $E \to 0$ and have a regular expansion in powers of the small parameter $\alpha^2 E^2$.

We have also considered interference corrections due to diagrams with two and three intersecting impurity lines. These interference terms are dominant in comparison with the semiclassical result and also non-analytic in the limit $E \to 0$. Density of states includes an extra ultraviolet logarithmic correction (4.15) as compared to the mean-field result (3.8). Conductivity acquires a leading universal (independent of the disorder strength) correction $\propto |E|$ and two subleading corrections with the ultraviolet and infrared logarithms (4.34). The leading correction to the conductivity is due to the diagrams with two crossed impurity lines while the subleading logarihmic terms also include a contribution from the diagrams with three crossed impurities. Our results produce a prediction for the concentration dependence of conductivity (4.36) that can be directly checked in an experiment.

It is worth mentioning some similarities between our results and interference corrections in a conventional metal with parabolic spectrum studied in Refs. [43, 44]. The leading correction in both models is of a relative strength $\alpha E \sim (E\tau)^{-1}$ and comes from the same two diagrams Fig. 4.2(a,c). The subleading correction with the infrared logarithm has a relative strength $(\alpha E)^2 \ln(\alpha E) \sim (E\tau)^{-2} \ln(E\tau)$. In a conventional metal it comes from all three diagrams with two crossed impurities Fig. 4.2 and in addition from four diagrams Fig. 4.5(a–d). In a Weyl semimetal only the latter four diagrams provide this correction. Finally, the ultraviolet logarithmic correction $\sim (\alpha E)^2 \ln(E/\Delta)$ comes from almost all interference diagrams with two and three impurities considered in this work, while in the case of conventional metal such a correction appears only in two diagrams Fig. 4.2c and Fig. 4.5h. Ultraviolet logarithm cancels in the expression for electron mobility $\mu = \sigma/(en)$ in a conventional metal model while for the Weyl semimetal such a cancellation does not occur.

The model of the random potential disorder can be directly generalized to include a possible random vector potential. This will lead to appearance of two distinct disorder parameters instead of a single quantity α. The whole calculation scheme developed in this work can be applied to this more general model with minimal modifications. While the number of relevant diagrams will increase dramatically (each impurity line will be of either scalar or vector type), we expect that qualitative results of our calculation will still hold. Only the coefficients in the expansion (4.34) will be modified. This more general model will be the subject of a separate study.

A Polarization operator

In this Appendix we discuss the momentum integral which involves denominators of two Green functions in an arbitrary dimension d. By analogy, we name such an integral polarization operator. Calculation of the polarization operator starts with the standard Feynmann trick that allows us to combine the two denominators into a single one at the cost of introducing an auxiliary integral over the Feynmann parameter x. After that, d-dimensional integration over momentum is straightforward. In the Matsubara formalism, we thus obtain the following expression for the polarization operator:

$$I(i\epsilon_1, i\epsilon_2, q) = \int \frac{p^{d-1}\,dp}{[\epsilon_1^2 + (\mathbf{p}+\mathbf{q})^2][\epsilon_2^2 + p^2]} = \int_0^1 dx \int \frac{p^{d-1}\,dp}{[x\epsilon_1^2 + (1-x)\epsilon_2^2 + p^2 + x(1-x)q^2]^2}$$
$$= \frac{\pi(2-d)}{4\sin(\pi d/2)} \int_0^1 dx \left[x\epsilon_1^2 + (1-x)\epsilon_2^2 + x(1-x)q^2\right]^{d/2-2}. \quad \text{(A.1)}$$

Parameters $\epsilon_{1,2}$ are assumed real and positive.

The indefinite integral over x can be expressed through the hypergeometric function with the help of the following identity:

$$\int dx\,(x-a)^s(b-x)^s = \text{const} - \frac{(b-a)^s(b-x)^{s+1}}{s+1} F\left(s+1, -s, s+2, \frac{b-x}{b-a}\right)$$
$$= \text{const} + \frac{1}{2}(x-a)^s(b-x)^s(2x-a-b) F\left(1, -s, \frac{3}{2}, -\frac{(2x-a-b)^2}{4(x-a)(b-x)}\right). \quad \text{(A.2)}$$

Here a and b correspond to the roots of the integrand in Eq. (A.1). It is easy to check that $a < 0$ and $b > 1$. The first expression in Eq. (A.2) follows from the basic integral representation of the hypergeometric function [48, Eq. 15.6.1]. More symmetric second expression is a result of the quadratic transformation [48, Eq. 15.8.19] followed by the linear transformation [48, Eq. 15.8.2]. [Note that arbitrary constants in the two forms of Eq. (A.2) are different.] The argument of the hypergeometric function in the latter expression of Eq. (A.2) remains finite and negative everywhere for $0 < x < 1$. Hence this indefinite integral can be used directly to evaluate Eq. (A.1) by taking the difference of its values between $x = 1$ and $x = 0$.

$$I(i\epsilon_1, i\epsilon_2, q) = M(i\epsilon_1, i\epsilon_2, q) + M(i\epsilon_2, i\epsilon_1, q), \quad \text{(A.3)}$$

$$M(i\epsilon_1, i\epsilon_2, q) = \frac{\pi(2-d)\epsilon_1^{d-4}}{8q^2\sin(\pi d/2)}\left(q^2 - \epsilon_1^2 + \epsilon_2^2\right) F\left(1, 2-\frac{d}{2}, \frac{3}{2}, -\frac{(q^2-\epsilon_1^2+\epsilon_2^2)^2}{4\epsilon_1^2 q^2}\right). \quad \text{(A.4)}$$

This is the most compact explicit expression of the polarization operator for arbitrary d. However, it is not well-suited to analyze the limit of large q, that is needed to properly apply dimensional regularization. Hence we perform the transformation [48, Eq. 15.8.2] with the

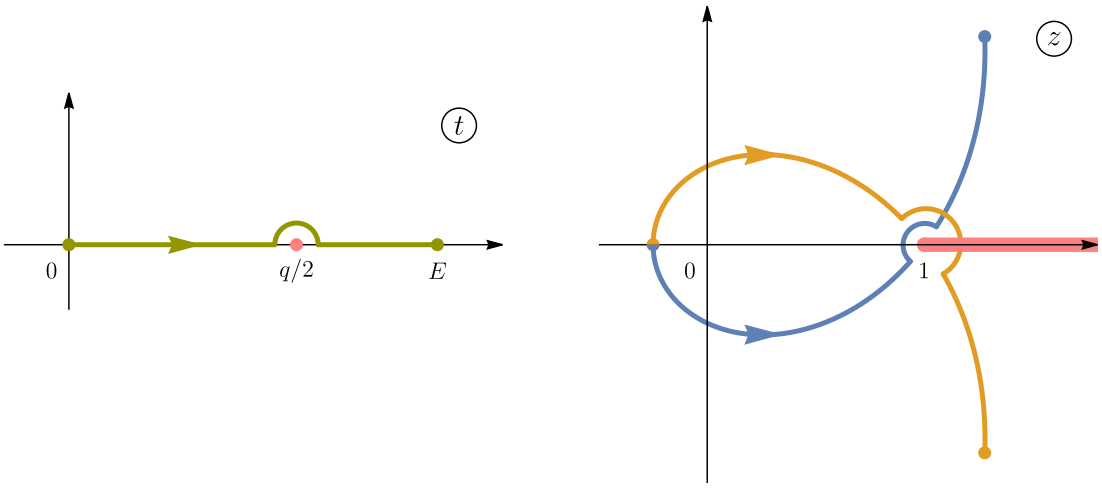

Figure A.1: Left: Transformation of variables for analytic continuation $i\epsilon_{1,2} = i\gamma \pm t$ in the calculation of I_{RA}. For large energies, the point $t = q/2$ should be bypassed to avoid the branch point of the hypergeometric function in Eq. (A.5). Right: Corresponding transformation of the argument of the hypergeometric function. Two curves correspond to $M(\epsilon_1, \epsilon_2)$ and $M(\epsilon_2, \epsilon_1)$. One of these two contours always intersect the branch cut of the hypergeometric function $[1, +\infty)$.

function M and obtain its alternative form:

$$M(i\epsilon_1, i\epsilon_2, q) = \frac{\pi}{2\sin(\pi d/2)}\left[\frac{\epsilon_1^{d-2}}{q^2-\epsilon_1^2+\epsilon_2^2}F\left(1,\frac{1}{2},\frac{d}{2},-\frac{4\epsilon_1^2q^2}{(q^2-\epsilon_1^2+\epsilon_2^2)^2}\right)\right.$$
$$\left. - \frac{\Gamma^2(d/2)}{\Gamma(d-1)}q^{2-d}\left[\left(q^2+\epsilon_1^2+\epsilon_2^2\right)^2-4\epsilon_1^2\epsilon_2^2\right]^{(d-3)/2}\operatorname{sgn}\left(q^2-\epsilon_1^2+\epsilon_2^2\right)\right]. \quad \text{(A.5)}$$

With the two results for $M(i\epsilon_1, i\epsilon_2, q)$, we can readily find the polarization operator with two Green functions of the same kind. This amounts to setting $\epsilon_1 = \epsilon_2 = \epsilon$ and performing analytical continuation in the upper complex half-plane $i\epsilon \mapsto i\gamma \pm E$. (Here we include the real part of the self-energy into E while keeping the imaginary part γ explicit.) This yields two equivalent expressions for $I_{RR/AA}$ suitable for small or large q expansion:

$$I_{RR/AA}(q) = \frac{\pi(2-d)}{4\sin(\pi d/2)}(\gamma \mp iE)^{d-4}F\left(1,2-\frac{d}{2},\frac{3}{2},\frac{q^2}{4(E\pm i\gamma)^2}\right)$$
$$= \frac{\pi}{\sin(\pi d/2)}\left[\frac{(\gamma\mp iE)^{d-2}}{q^2}F\left(1,\frac{1}{2},\frac{d}{2},\frac{4(E\pm i\gamma)^2}{q^2}\right)\right.$$
$$\left. - \frac{\Gamma^2(d/2)}{q\,\Gamma(d-1)}\left[q^2-4(E\pm i\gamma)^2\right]^{(d-3)/2}\right]. \quad \text{(A.6)}$$

The case of mixed retarded-advanced polarization operator is much more subtle. Analytic continuation in two different energy parameters can be performed as follows. We set $i\epsilon_{1,2} = i\gamma \pm t$ and continuously change t from 0 to E. At the initial value $t = 0$, both energies $\epsilon_{1,2}$ are positive and equal. Hence the Matsubara expression (A.5) applies and the signum function in the last term is 1. For relatively low energies $E < q/2$, we can analytically continue t directly along the real axis and reach the point $t = E$. Substituting the end point of this trajectory into Eq. (A.5) yields the result for M and hence for I_{RA}.

For larger energies, the argument of the hypergeometric function in Eq. (A.5) becomes 1 when t reaches the value $q/2$. This is a branch point of the hypergeometric function (its branch cut runs from 1 to $+\infty$) hence it should be bypassed. We will assume that t circumvents the point $q/2$ from above in the complex plane on its way to $t = E > q/2$. Then the argument of the hypergeometric function in $M(i\epsilon_1, i\epsilon_2, q)$ circumvents the branch point 1 from the left (see Fig. A.1) and we remain on the same principal branch of the hypergeometric function. But at the same time in the second term $M(i\epsilon_2, i\epsilon_1, q)$ of Eq. (A.3), the argument of the hypergeometric function evolves along the (almost) complex conjugate path, it circumvents the branch point 1 from the right and crosses the branch cut (see Fig. A.1). This means that we should add the value of the jump across the branch cut [48, Eq. 15.2.3] in order to stay on the principal branch. Adding together $M(i\gamma+E, i\gamma-E, q)$ and $MM(i\gamma - E, i\gamma + E, q)$, we represent the polarization operator I_{RA} as

$$I_{RA}(q) = \frac{\pi}{2\sin(\pi d/2)}\left[\left(\frac{(\gamma - iE)^{d-2}}{q^2 + 4iE\gamma} F\left(1, \frac{1}{2}, \frac{d}{2}, \frac{4(E+i\gamma)^2 q^2}{(q^2+4iE\gamma)^2}\right) + \{E \mapsto -E\}\right) - \frac{2\Gamma^2(d/2)}{\Gamma(d-1)} q^{2-d}\Big[\big(q^2 - 4E^2\big)\big(q^2 + 4\gamma^2\big)\Big]^{(d-3)/2}\theta(q-2E)\right]. \quad \text{(A.7)}$$

This expression is equally well suited for both small and large q expansion. Let us note that the same result can be obtained if we bypass the branch point in t from the other side (from below). The only difference is that the roles of the two terms in Eq. (A.3) are interchanged.

We have so far established exact expressions for the polarization operator for any values of the parameters E, γ, and q and for arbitrary d. For the computation of diagrams, we are mostly interested in the 3D limit. More specifically, deviations from $d = 3$ should be taken into account only in the limit $q \gg E$ where dimensional regularization is applied. This means we can substitute $d = 3$ in Eqs. (A.6) and (A.7) everywhere except the last terms where we keep q^{d-3} asymptotics. This yields the following simplified versions of the polarization operators:

$$I_{RA}(q) = \frac{\pi}{2q}\left(\frac{\pi}{2}\, q^{d-3} - E^{d-3} \arctan\frac{2\gamma}{q}\right), \quad \text{(A.8a)}$$

$$I_{RR/AA}(q) = \frac{\pi}{2q}\left(\frac{\pi}{2}\, q^{d-3} - E^{d-3} \arctan\frac{2\gamma \mp 2iE}{q}\right). \quad \text{(A.8b)}$$

Bibliography

[1] P. A. M. Dirac, *The quantum theory of the electron*, Proc. R. Soc. Lond. A **117**, 610 (1928).

[2] H. Weyl, *Gravitation and the electron*, PNAS **15**, 323 (1929).

[3] Y. Fukuda et al., *Measurements of the Solar Neutrino Flux from Super-Kamiokande's First 300 Days*, Phys. Rev. Lett. **81**, 1158 (1998).

[4] H. Nielsen and M. Ninomiya, *The Adler-Bell-Jackiw anomaly and Weyl fermions in a crystal*, Phys. Lett. B **130**, 389 (1983).

[5] L. Balents, *Weyl electrons kiss*, Physics **4**, 36 (2011).

[6] X. Wan, A. M. Turner, A. Vishwanath, and S. Y. Savrasov, *Topological semimetal and Fermi-arc surface states in the electronic structure of pyrochlore iridates*, Phys. Rev. B **83**, 205101 (2011).

[7] N. P. Armitage, E. J. Mele, and A. Vishwanath, *Weyl and Dirac semimetals in three-dimensional solids*, Rev. Mod. Phys. **90**, 015001 (2018).

[8] B. Q. Lv, H. M. Weng, B. B. Fu, X. P. Wang, H. Miao, J. Ma, P. Richard, X. C. Huang, L. X. Zhao, G. F. Chen, Z. Fang, X. Dai, T. Qian, and H. Ding, *Experimental Discovery of Weyl Semimetal TaAs*, Phys. Rev. X **5**, 031013 (2015).

[9] H. Weng, C. Fang, Z. Fang, B. A. Bernevig, and X. Dai, *Weyl Semimetal Phase in Noncentrosymmetric Transition-Metal Monophosphides*, Phys. Rev. X **5**, 011029 (2015).

[10] B. Sbierski, G. Pohl, E. J. Bergholtz, and P. W. Brouwer, *Quantum transport of disordered Weyl semimetals at the nodal point*, Phys. Rev. Lett. **113**, 026602 (2014).

[11] M. Trescher, B. Sbierski, P. W. Brouwer, and E. J. Bergholtz, *Tilted disordered Weyl semimetals*, Phys. Rev. B **95**, 045139 (2017).

[12] S. V. Syzranov, V. Gurarie, and L. Radzihovsky, *Unconventional localization transition in high dimensions*, Phys. Rev. B **91**, 035133 (2015).

[13] S. V. Syzranov, L. Radzihovsky, and V. Gurarie, *Critical transport in weakly disordered semiconductors and semimetals*, Phys. Rev. Lett. **114**, 166601 (2015).

[14] B. Roy and S. Das Sarma, *Diffusive quantum criticality in three-dimensional disordered Dirac semimetals*, Phys. Rev. B **90**, 241112 (2014).

[15] S. V. Syzranov, P. M. Ostrovsky, V. Gurarie, and L. Radzihovsky, *Critical exponents at the unconventional disorder-driven transition in a Weyl semimetal*, Phys. Rev. B **93**, 155113 (2016).

[16] E. Fradkin, *Critical behavior of disordered degenerate semiconductors. 1. Models, symmetries, and formalism*, Phys. Rev. B **33**, 3257 (1986).

[17] E. Fradkin, *Critical behavior of disordered degenerate semiconductors. 2. Spectrum and transport properties in mean-field theory*, Phys. Rev. B **33**, 3263 (1986).

[18] A. Altland and D. Bagrets, *Effective field theory of the disordered Weyl semimetal*, Phys. Rev. Lett. **114**, 257201 (2015).

[19] R. Nandkishore, D. A. Huse, and S. L. Sondhi, *Rare region effects dominate weakly disordered three-dimensional Dirac points*, Phys. Rev. B **89**, 245110 (2014).

[20] T. Holder, C.-W. Huang, and P. M. Ostrovsky, *Electronic properties of disordered Weyl semimetals at charge neutrality*, Phys. Rev. B **96**, 174205 (2017).

[21] M. Buchhold, S. Diehl, and A. Altland, *Vanishing density of states in weakly disordered Weyl semimetals*, Phys. Rev. Lett. **121**, 215301 (2018).

[22] Y. Ominato and M. Koshino, *Quantum transport in a three-dimensional Weyl electron system*, Phys. Rev. B **89**, 054202 (2014).

[23] J. Klier, I. V. Gornyi, and A. D. Mirlin, *From weak to strong disorder in Weyl semimetals: Self-consistent Born approximation*, Physical Review B **100**, 125160 (2019).

[24] J. H. Pixley and J. H. Wilson, *Rare regions and avoided quantum criticality in disordered Weyl semimetals and superconductors*, Ann. Phys. **435**, 168455 (2021).

[25] D. Gross and A. Neveu, *Dynamical symmetry breaking in asymptotically free field theories*, Phys. Rev. D **10**, 3235 (1974).

[26] A. Bondi, G. Curci, G. Paffuti, and P. Rossi, *Metric and central charge in the perturbative approach to 2-dimensional fermionic models*, Ann. Phys. **199**, 268 (1990).

[27] J. A. Gracey, T. Luthe, and Y. Schröder, *Four loop renormalization of the Gross-Neveu model*, Phys. Rev. D **94**, 125028 (2016).

[28] B. Rosenstein, B. Warr, and S. Park, *4-fermion theory is renormalizable in* $2 + 1$ *dimensions*, Phys. Rev. Lett. **62**, 1433 (1989).

[29] K. S. Novoselov, A. K. Geim, S. V. Morozov, D. Jiang, Y. Zhang, S. V. Dubonos, I. V. Grigorieva, and A. A. Firsov, *Electric field effect in atomically thin carbon films*, Science **306**, 666 (2004).

[30] K. Novoselov, A. Geim, S. Morozov, D. Jiang, M. Katsnelson, I. Grigorieva, S. Dubonos, and A. Firsov, *Two-dimensional gas of massless Dirac fermions in graphene*, Nature **438**, 197 (2005).

[31] Y. Zhang, J. P. Small, M. E. S. Amori, and P. Kim, *Electric Field Modulation of Galvanomagnetic Properties of Mesoscopic Graphite*, Phys. Rev. Lett. **94**, 176803 (2005).

[32] Y. B. Zhang, Y. W. Tan, H. L. Stormer, and P. Kim, *Experimental observation of the quantum Hall effect and Berry's phase in graphene*, Nature **438**, 201 (2005).

[33] C. Berger, Z. M. Song, T. B. Li, X. B. Li, A. Y. Ogbazghi, R. Feng, Z. T. Dai, A. N. Marchenkov, E. H. Conrad, P. N. First, and W. A. de Heer, *Ultrathin epitaxial graphite: 2D electron gas properties and a route toward graphene-based nanoelectronics*, J. Phys. Chem. B **108**, 19912 (2004).

[34] I. L. Aleiner and K. B. Efetov, *Effect of disorder on transport in graphene*, Phys. Rev. Lett. **97**, 236801 (2006).

[35] P. M. Ostrovsky, I. V. Gornyi, and A. D. Mirlin, *Electron transport in disordered graphene*, Phys. Rev. B **74**, 235443 (2006).

[36] A. Schuessler, P. M. Ostrovsky, I. V. Gornyi, and A. D. Mirlin, *Analytic theory of ballistic transport in disordered graphene*, Phys. Rev. B **79**, 075405 (2009).

[37] V. S. Dotsenko, *Critical behavior of the phase transition in the 2D Ising model with impurities*, Adv. Phys. **32**, 129 (1983).

[38] A. W. W. Ludwig, M. P. A. Fisher, R. Shankar, and G. Grinstein, *Integer quantum Hall transition: An alternative approach and exact results*, Phys. Rev. B **50**, 7526 (1994).

[39] A. A. Nersesyan, A. M. Tsvelik, and F. Wenger, *Disorder effects in 2-dimensional d-wave superconductors*, Phys. Rev. Lett. **72**, 2628 (1994).

[40] A. Altland, B. D. Simons, and M. R. Zirnbauer, *Theories of low-energy quasi-particle states in disordered d-wave superconductors*, Phys. Rep. **359**, 283 (2002).

[41] M. Z. Hasan and C. L. Kane, *Colloquium: Topological insulators*, Rev. Mod. Phys. **82**, 3045 (2010).

[42] J. Zinn-Justin, *Quantum Field Theory and Critical Phenomena* (Oxford University Press, 2002).

[43] T. R. Kirkpatrick and D. Belitz, *Nonanalytic behavior of ultrasonic-attenuation in disordered electronic systems*, Phys. Rev. B **34**, 2168 (1986).

[44] K. I. Wysokinski, W. Park, D. Belitz, and T. R. Kirkpatrick, *Density expansion for the mobility in a quantum Lorentz model*, Phys. Rev. E **52**, 612 (1995).

[45] M. Peskin and D. Schroeder, *An Introduction to Quantum Field Theory* (Westview Press, 1995).

[46] F. Evers and A. D. Mirlin, *Anderson transitions*, Rev. Mod. Phys. **80**, 1355 (2008).

[47] L. Gor'kov, A. Larkin, and D. Khmel'nitskii, *Particle conductivity in a two-dimensional random potential*, JETP Lett. **30**, 228 (1979).

[48] *NIST Digital Library of Mathematical Functions*, edited by F. W. J. Olver, A. B. Olde Daalhuis, D. W. Lozier, B. I. Schneider, R. F. Boisvert, C. W. Clark, B. R. Miller, B. V. Saunders, H. S. Cohl, and M. A. McClain, http://dlmf.nist.gov/.